In Vitro and Ex Vivo Investigation of the Effects of Polydopamine Nanoparticle Size on Their Antioxidant and Photothermal Properties: Implications for Biomedical Applications

ACS APPLIED NANO MATERIALS

www.acsanm.org Article

In Vitro and Ex Vivo Investigation of the Effects of Polydopamine Nanoparticle Size on Their Antioxidant and Photothermal Properties: Implications for Biomedical Applications

Alessio Carmignani,* Matteo Battaglini, Edoardo Sinibaldi, Attilio Marino, Veronica Vighetto, Valentina Cauda, and Gianni Ciofani*

Cite This: *ACS Appl. Nano Mater.* 2022, 5, 1702−1713 Read Online

ACCESS | Metrics & More | Article Recommendations | Supporting Information

ABSTRACT: Polydopamine (PDA) is a polymer that derives from the self-polymerization of the biomolecule dopamine. It can be easily synthesized to obtain spherical nanoparticles (PDNPs), tunable in terms of size, loaded cargo, and surface functionalization. PDNPs have been increasingly attracting the attention of the research community due to their elevated versatility in the biomedicine field, for their excellent ability to encapsulate drugs, to convert near-infrared (NIR) radiation into heat, and to act as an antioxidant agent. Size is an important aspect to be considered, especially concerning the specific intended field of application. This work aims at investigating how changes in the size of PDNPs affect the nanoparticle properties relevant for biomedical applications, especially focusing on cancer nanomedicine. A library of differently sized PDNPs (from 145 to 957 nm) has been obtained by varying the ammonia/dopamine molar ratio during the synthesis procedure, and detailed characterization in terms of biocompatibility, cell internalization, antioxidant capacity, and photothermal conversion has been carried out. Experiments showed that nanoparticles with a larger diameter display higher NIR absorbance, superior resistance to degradation, and higher photothermal conversion capacity (the latter confirmed by a mathematical model). On the other hand, a reduction in diameter size induces both improved antioxidant properties and enhanced cellular uptake. Herein, we provide a useful tool, allowing one to choose the proper size of PDNPs tailored for specific biomedical applications.

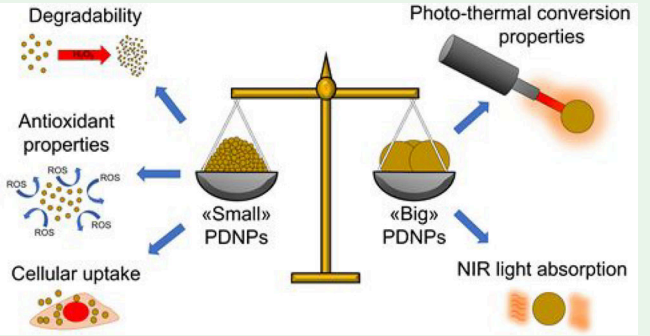

KEYWORDS: *polydopamine nanoparticles, size effects, antioxidant nanostructures, photothermal effect, computational modeling*

INTRODUCTION

Polydopamine (PDA) derives from the self-polymerization of dopamine, a molecule belonging to the catecholamine family, chemical compounds deriving from the amino acid tyrosine.[1] This molecule shows unique chemical properties that have recently attracted consistent attention in the biomedical field. Its chemical structure, very similar to that one of melanin, makes PDA a biocompatible and biodegradable polymer.[2] These features are essential for biomedical applications, already widely investigated, both in vitro and in vivo.[3−7] Starting from an adaptation of the Stöber reaction, dopamine can be easily used to prepare polydopamine nanoparticles (PDNPs).[8]

These spherical structures are easily tunable in terms of size by varying the ammonia/dopamine molar ratio within the synthesis mixture.[9,10] PDNPs represent a very promising multitasking tool exploited in several biomedical fields;[11−13] for example, they represent an optimal compromise between inorganic and organic antioxidant materials, being a fully organic, biocompatible, and biodegradable structure with exceptional antioxidant abilities given by the presence on the surface of functional groups like catechol, imine, and amine.[11,14] These abilities have provided promising results in the treatment of acute inflammations, for example, occurring in periodontal diseases.[8,14,15] A further interesting aspect of PDA-based nanostructures is their capacity to convert the near-infrared (NIR) radiation into thermal energy, thus generating heat. This is a recently investigated aspect of PDA with still a few applications, mainly focused on the photothermal ablation of cancer cells;[16−18] by fine tuning the NIR irradiation, we have moreover demonstrated the possibility to stimulate neuronal activity.[19] These structures can also be easily used to encapsulate drugs, and owing to their aforementioned functional groups,

Received: December 28, 2021
Accepted: January 4, 2022
Published: January 14, 2022

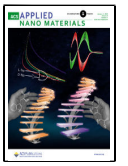

their surface can be functionalized with specific ligands that promote selective targeting and biological barrier passage.[11,20]

This work aims at optimizing the PDNP size according to the intended use, i.e., for effective antioxidant therapy, chemotherapy, drug delivery, or photothermal treatment. Accordingly, the nanomaterial is required to be efficiently internalized by the cells and to show high levels of biocompatibility; moreover, depending on the specific application, the nanomaterial is required to possess high antioxidant properties and/or photothermal conversion abilities. In this work, the size of PDNPs has been finely tuned by varying the ammonia/dopamine molar ratio during synthesis, and the effects of size on the nanoparticle properties and nanoparticle interactions with cells have been carefully investigated.

EXPERIMENTAL SECTION

2.1. Polydopamine Nanoparticles Synthesis. By following an adaptation of the well-known Stöber reaction (Bao et al.), PDNPs were synthesized exploiting dopamine polymerization (Figure 1).[8] A 90 mL

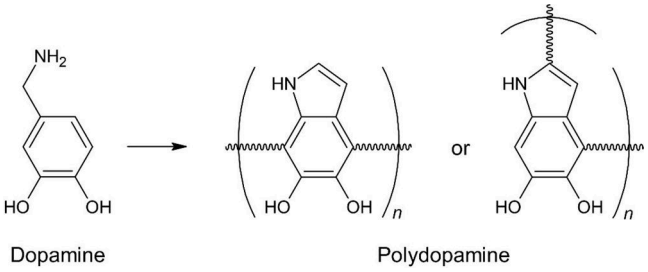

Figure 1. Chemical structure of dopamine, and suggested mechanism of polydopamine polymerization.

amount of Milli-Q water and 40 mL of ethanol were mixed under mild stirring at room temperature for 30 min with ammonium hydroxide solution (Carlo Erba). To modulate the nanoparticle size, eight different ammonia/dopamine molar ratios were taken into consideration (23.20, 17.40, 14.50, 11.60, 8.70, 5.80, 4.35, and 2.9). Then, 0.5 g of dopamine hydrochloride (Sigma) previously dissolved in 10 mL of Milli-Q water was added to the mixture. The reaction was left under stirring for 24 h; formed nanoparticles were thereafter diluted 1:1 in ethanol and then centrifuged at 8960*g* for 30 min at 4 °C. A pellet was collected and resuspended in Milli-Q water for 3 subsequent rinsing steps: the first one at 8960*g*; the second and the third ones at 12 000*g*. PDNP concentrations were quantified by weighting selected lyophilized aliquots.

For internalization purposes and for evaluation of the intracellular heating, DiO-stained and DiI-stained PDNPs were prepared. Ten micromolar DiO (Vybrant Multicolor Cell-Labeling Kit, Thermo Fisher Scientific) was added to 1 mL of Milli-Q water containing 5 mg/mL nanoparticles and left under stirring for 2 h. The dispersion was then washed three times with Milli-Q water through centrifugation at 16 602*g*. An analogous procedure was followed using 10 μM DiI (Vybrant Multicolor Cell-Labeling Kit, Thermo Fisher Scientific).

2.2. Scanning Electron Microscopy. The size and morphology of the nanoparticles have been determined through scanning electron microscopy (SEM) analysis and exploiting Gwyddion software. For each of the eight nanoparticle classes, 10 μL of a 100 μg/mL suspension was placed on a silicon substrate and let dry under a chemical hood. After gold sputtering using a Quorum Tech Q150RES Gold Sputter Coater (30 mA for 60 s), images of the samples were acquired using a dual-beam SEM system, Helios NanoLab 600i FIB/SEM, FEI.

2.3. Dynamic Light Scattering. Nanoparticles were characterized through dynamic light scattering (DLS) measurements in terms of average hydrodynamic diameter (D_h), polydispersity index (PDI), and average surface zeta potential (ζ-pot) using a Malvern Zetasizer Nano ZS90. D_h and PDI measurements were performed on 100 μg/mL PDNPs placed in polystyrene cuvettes. ζ-Pot measurements were performed on 100 μg/mL PDNPs in a 10 mM NaCl solution placed in folded capillary cells (Malvern Zetasizer Nano series). A short-term stability analysis on 100 μg/mL PDNPs, either in water (Milli-Q water for D_h values and 10 mM NaCl solution for ζ-pot) or in 5% hydrogen peroxide (H_2O_2), was carried out by acquisition of D_h and ζ-pot values over 1 h. In order to evaluate the effects of nanoparticle degradation on the D_h values, analyses on 100 μg/mL nanoparticles incubated at 37°C in a 5% H_2O_2 solution were performed at different time points (0, 24, 48, and 72 h).

2.4. UV−vis Spectroscopy. Absorbance at 808 nm of aqueous dispersions of PDNPs was acquired with a PerkinElmer UV/vis spectrophotometer (Lambda 45). Analyses were carried out also at different time points (0, 24, 48, and 72 h) during incubation of 100 μg/mL nanoparticles at 37°C in a 5% H_2O_2 solution, in order to assess any effects of nanoparticle degradation on NIR radiation absorption.

2.5. Electron Paramagnetic Resonance. Electron paramagnetic resonance (EPR) spectroscopy coupled with the spin-trapping technique was used to analyze the antioxidant activity of PDNPs at various sizes. The Fenton reaction was generated in situ for each sample, and free hydroxyl radicals present in the sample were trapped using DMPO (Sigma) as spin trap, as reported in a previous work.[19] The tested solutions were composed of H_2O_2 (20 μL, 10 mM), DMPO (100 μL, 50 mM), aqueous dispersion of different nanoparticles (78 μL) with a final concentration of PDNPs equal to 500 μg/mL, and $FeSO_4{\cdot}7H_2O$ (2 μL, 10 mM). Each sample was prepared and mixed in an Eppendorf tube. The resulting solution was then transferred into a quartz microcapillary tube and placed in the EPR cavity for measurement. EPR spectra were recorded on a Bruker EMXnano X-Band spectrometer (Bruker). The instrument was set to have a frequency of 9.74 GHz, a receiver gain of 60 dB, and a sweep time of 90 s. Spectral elaboration was performed using the Bruker Xenon software (Bruker) for baseline correction, and the total number of hydroxyl radicals trapped was quantified using the SpinFit software (Bruker).

2.6. Photothermal Conversion Ability. The ability of PDNPs to convert NIR light into heat was evaluated using an RLTMDL-808-500 NIR laser (λ = 808 nm, 2.5 mm of spot diameter, 120 s of irradiation) and a FLIR thermal camera (A300) to acquire thermal data. For each differently sized class of nanoparticles, tests were performed in a WillCo dish (WillCo Wells) using aqueous dispersions with increasing concentrations of PDNPs (100, 250, 500, and 1000 μg/mL), with the laser source set at the maximum power (541 mW). In order to keep the temperature stable during the experiment, the aforementioned WillCo dish was placed inside a 120 mm Petri dish (Anicrin) filled with water and placed on a heating plate set at 37°C (room temperature of about 25°C). For each experimental condition, data were acquired three times.

The PDNP photothermal conversion ability was also assessed in postmortem vertical slices of cow brain tissue obtained from a local butcher and embedded in agarose gel. For each differently sized class of nanoparticles, 25 μg of PDNPs was injected 2 mm below the surface of the tissue with the laser source (λ = 808 nm, 2.5 mm of spot diameter, 120 s of irradiation) set at five different powers (57, 163, 274, 385, and 541 mW). For each experimental condition, data were acquired three times.

Over the entire irradiation period, thermal data were collected along a straight segment having the NIR spot center as the midpoint of the stimulation bench. Specifically, for in vitro tests, data were collected along a top-surface diameter of the WillCo dish, whereas a line on the vertical sample surface was considered for ex vivo tests. For each acquisition, raw data were postprocessed to obtain graphs of the temperature along the designed segment. For each experimental condition, values of the average temperature increment ($\overline{\Delta T}$) in the selected experimental domain were obtained according to eq 1

$$\overline{\Delta T} = \frac{\int_0^R \Delta T(x)\mathrm{d}x}{R} \quad (1)$$

where $\Delta T(x)$ is the increment of temperature detected along a linear domain (please see in the following for details), while R is the

https://doi.org/10.1021/acsanm.1c04536
ACS Appl. Nano Mater. 2022, 5, 1702−1713

considered domain length (i.e., 2.5 cm for in vitro tests and 1.0 cm for ex vivo tests). Furthermore, by leveraging symmetry, two data sets were derived from each measure over the WillCo dish diametric span (by half-splitting) to obtain mean ± standard deviation experimental data later used for calibrating the associated computational model (see below).

2.7. Computational Model. A computational model was introduced in order to derive quantitative insights from the aforementioned in vitro irradiation tests on the photothermal conversion capability. More specifically, starting from the geometry of the exploited commercial dishes and based on the alignment of the NIR irradiation direction with the symmetry axis of said dishes, a 2D axisymmetric approximation was adopted to contain computational costs. Both photothermal conversion in the WillCo dish domain (i.e., in the aqueous dispersion containing PDNPs) and heat transfer in the whole domain were simultaneously modeled by leveraging the multiphysics modeling capabilities of the adopted finite element solver (Comsol Multiphysics, by COMSOL Inc.).

Multiphysics coupling was implemented as follows. NIR irradiation was introduced as a boundary condition, namely, a W_{NIR} = 541 mW power on the [0, 12.5] mm radial span (one-half of the NIR spot diameter). Radiation intensity through the dispersion was assumed to decrease due to absorption according to the widely adopted Lambert–Beer law.[21] An absorption coefficient $\tilde{\alpha}$ (with physical units m^{-1}), depending on the specific PDNP diameter and on the concentration at hand, was thus introduced to be later determined based on the experimental data (see below). At any location in the dispersion domain, the absorbed energy was then introduced as a source term for the heat transfer problem, thus complementing thermal conduction and diffusion in the related governing equation. Material properties for both dishes were defined by considering polystyrene data (~1.5×10^3 J kg^{-1} K^{-1} specific heat capacity[22]) and, in particular, datasheet figures (1.06 g cm^{-3} density, 3.9×10^{-2} W m^{-1} K^{-1} thermal conductivity), whereas common parameter values for glass and water (the latter also used for the aqueous dispersion) were directly imported from the numerical solver libraries. A fixed temperature T_{plate} = 37°C was imposed on the bottom side of the Petri dish, and a convective flux $q = h(T - T_{room})$ was enforced on the remaining boundaries, facing air at T_{room} = 25°C. The effective heat transfer coefficient h in the above relation was determined based on the experimental data (see below) to contain experimental uncertainties. A triangular mesh was adopted for space discretization (by refining the mesh size up to obtaining discretization-independent results), and time integration was advanced up to the final irradiation time, namely, t = 120 s.

Numerical results (in terms of both numerical data and derived images) were exported from Comsol and further processed in the Matlab (The Mathworks Inc.) numerical environment. The aforementioned coefficients $\tilde{\alpha}$ and h were calibrated as follows. Four experimental data sets were considered, namely, those associated with both 204 and 522 nm PDNPs diameters at both 100 and 250 μg/mL concentrations. The related mean temperature at t = 120 s and over a [0, 6.5] mm radial span (one-half of the dish radius, to focus on PDNP conversion farther from the dish boundary) was taken as an experimental set. A double parameter sweep was run in Comsol: h (a single value) and $\tilde{\alpha}$ (four values, one for each diameter/concentration pair) were thus defined by minimizing the error (squared numerical difference, over the considered radial span) between the numerical and the experimental sets. Finally, taking as a reference value for $\tilde{\alpha}$ that associated with (204 nm/100 μg/mL), namely, the pair expected to heat the least, we finally derived a normalized absorption coefficient for ease of presentation.

2.8. Cell Culture. U-87 MG cells (ATCC HTB-14) and U-87 MG/GFP cells (Cellomics SC-1495) were cultured in proliferation conditions using high-glucose Dulbecco's modified Eagle medium (DMEM, Gibco) supplemented with 10% heat-inactivated fetal bovine serum (FBS, Gibco), 1% L-glutamine (stock 200 mM, Gibco), and 1% penicillin–streptomycin (100 IU/mL penicillin and 100 μg/mL streptomycin, Gibco). Cultures were maintained at 37°C in a humidity-saturated atmosphere with 5% of CO_2.

2.9. Cellular Viability. The effects on the viability of PDNPs of different sizes were evaluated on U-87 MG cells via the Quant-iT PicoGreen dsDNA Assay Kit (Invitrogen). For each of the eight different PDNP classes, cells were seeded at 10 000 cells/cm^2 density in a 96-well plate (Corning) and let adhere for 24 h. Then, cells were treated with increasing concentrations of PDNPs (0, 100, 250, and 500 μg/mL) and incubated for 72 h. Cells were thereafter washed in Dulbecco's phosphate-buffered saline (DPBS), suspended in 100 μL of Milli-Q water, and finally subjected to four cycles of freeze–thaw (from −80 to 37°C) in order to allow cell lysis and dsDNA release. Quant-iT PicoGreen dsDNA assay was carried out by mixing PicoGreen reagent, buffer, and cell lysate in Corning Costar 96-well black polystyrene plates following the manufacturer's instructions. Fluorescence was measured with a Victor X3 Multilabel Plate Reader (λ_{ex} = 360 nm, λ_{em} = 460 nm).

2.10. Cellular Internalization. Cellular uptake of PDNPs was evaluated via flow cytometry. U-87 MG cells were seeded at 10 000 cells/cm^2 density in a 24-well plate (Corning) and let adhere for 24 h. Then, cells were treated with 100 μg/mL of differently sized DiO-stained PDNPs and incubated for 72 h. After incubation, cells were washed in DPBS, detached from the wells, and analyzed with a CytoFLEX platform (Beckman Coulter, λ_{ex} = 488 nm, FITC λ_{em} = 525/40 nm, ECD λ_{em} = 610/20 nm).

Cellular uptake of PDNPs was evaluated also via confocal microscopy imaging. U-87 MG/GFP cells were seeded at 10 000 cells/cm^2 density in WillCo dishes and let adhere for 24 h. Then, cells were treated with 100 μg/mL of differently sized DiI-stained PDNPs and incubated for 72 h. After incubation, cells were washed in DPBS, fixed with 4% paraformaldehyde (PFA, Sigma-Aldrich) in DPBS at 4°C for 20 min, and washed twice with DPBS; nuclei were stained with 5 μg/mL Hoescht (Invitrogen). Confocal microscopy images were acquired with a C2s system (Nikon) equipped with a 60× oil immersion objective.

2.11. Intracellular Heating in U-87 MG Cells. The temperature increase upon PDNP incubation and NIR stimulation was quantified through confocal microscopy imaging by exploiting the temperature sensitivity of the DiI staining. For this purpose, cells were seeded at 10 000 cells/cm^2 density in WillCo dishes and let adhere for 24 h. Subsequently, cells were treated for 72 h with either 100 μg/mL DiI-stained 145 nm PDNPs or 100 μg/mL DiI-stained 957 nm PDNPs. During the NIR laser irradiation, cells were imaged through laser scanning confocal microscopy time-lapse imaging using a 20× objective and acquiring images every 15 s from three different fields. Cells were irradiated for 60 s with the laser source set at the maximum power (541 mW). The relative decrement in fluorescence intensity during NIR irradiation was calculated and expressed as F/F_0; the decrement in fluorescence of DiI-stained PDNPs was thereafter converted into temperature increment as described in ref 23; in particular, eq 2 was applied

$$\Delta F/F_0 = -0.0224\Delta T \quad (2)$$

2.12. Statistical Analysis. Statistical analysis was performed using the software *R*. Normality of data distributions was verified with the Shapiro–Wilk normality test. Normally distributed data were analyzed via ANOVA followed by the LSD posthoc test with Bonferroni correction and expressed as average ± standard deviation; non-normally distributed data were analyzed via the Kruskal–Wallis test followed by the Wilcox posthoc test with Holm correction and expressed as median ± 95% confidence interval. Each experiment was performed in triplicate (n = 3) if not differently indicated.

RESULTS AND DISCUSSION

3.1. PDNP Characterization. PDNPs were synthesized exploiting the Stöber reaction, and by changing the amount of ammonium hydroxide in each reaction solution, eight different classes of spherical nanoparticles were obtained.

First, morphological analyses were performed via SEM, and each of the eight different classes of nanoparticles showed a spherical shape and uniformity in terms of size and morphology

https://doi.org/10.1021/acsanm.1c04536
ACS Appl. Nano Mater. 2022, 5, 1702–1713

(Figure 2a). As previously mentioned, different nanoparticle diameters have been obtained by varying the ammonia/dopamine molar ratio in the synthesis solutions, from 23.20 to 2.90, and these diameters were calculated by analyzing previously mentioned SEM acquisitions (Figure 2b). DLS measurements performed on the differently sized PDNPs (from 145 ± 13 to 957 ± 48 nm) highlighted monodisperse/scarcely polydisperse distributions and strongly electronegative ζ-pot values (Figures S1 and S2). Furthermore, NIR absorption of the eight different classes of nanoparticles was assessed performing spectrophotometric analysis, and as expected, nanoparticles showed an increase in absorbance values at 808 nm along with their increment in diameter, ranging from 0.29 to 1.46 au for nanoparticles of 145 and 957 nm nominal diameter, respectively (Figure S3).[24,25] Nanoparticles with a 426 nm of diameter and larger (522, 710, and 957 nm) show a statistically significant increase in absorbance values with respect to smaller nanoparticles ($p < 0.001$, Table S1). In particular, moving from 299 to 426 nm, there is an increment in absorbance of 141%. All of these data are summarized in Table 1.

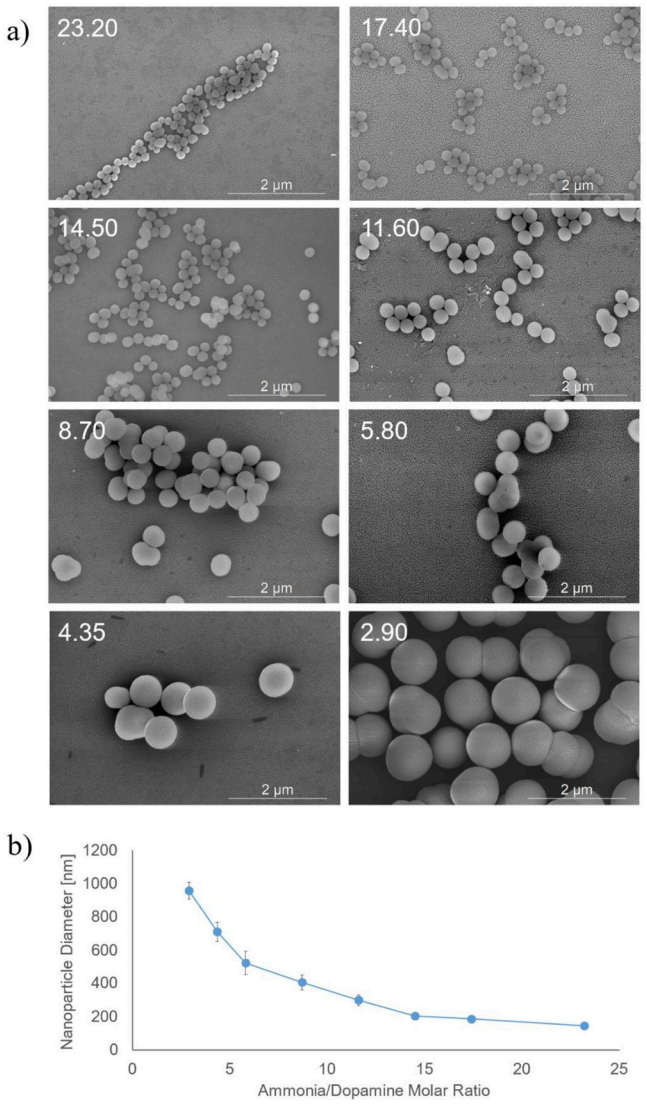

Figure 2. Morphological analysis of PDNPs at various sizes. (a) SEM images acquired at the same magnification with the ammonia/dopamine ratio values indicated. (b) Trend of the nanoparticle diameter along with the increment of the ammonia/dopamine ratio.

The results of the DLS measurements performed over 1 h, both in water and in 5% H_2O_2, showed that all eight differently sized PDNP classes remain stable during analysis, with no significant change in terms of D_h and ζ-pot. In particular, acquired values, related to $t = 0$ min, are all in a range of ±8% (Figure S4).

3.2. Nanoparticle Degradation. Depending on the intracellular compartment where nanoparticles are internalized, such as lysosomes and late endosomes, PDNPs can interface to an intracellular microenvironment with high levels of reactive oxygen species (ROS), like H_2O_2.[26] Furthermore, several pathologies, such as neurodegenerative disease, are characterized by severe intracellular levels of oxidative stress (OS), mainly associated with failure in ROS scavenging.[27,28] PDNPs, thanks to their excellent antioxidant properties, represent suitable agents for the treatment of cells showing an overproduction of ROS. To mimic these particular conditions, the degradation behavior of the eight PDNP classes was assessed in 5% H_2O_2.[29] Degradation analysis was performed through spectrophotometric and DLS measurements at different time points (0, 24, 48, and 72 h) during incubation. At 72 h, the absorbance at 808 nm of the larger nanoparticles (957 nm) showed a decrement of 19.8% compared to $t = 0$ h; this difference progressively increases with decreasing nanoparticle size: the smallest nanoparticles (145 nm PDNPs) show a 68.0% decrease in absorbance. Analogously, the size of the largest nanoparticles decreased of 16.7% after 72 h, while that of the smallest PDNPs decreased of 38.5%, confirming a better resistance of larger PDNPs to degradation in an oxidative environment.

Our results suggest that a higher surface/volume ratio appears to promote nanoparticle degradation (Figure S5), in line with the literature.[30,31] Recent evidences supporting the observed behavior include the work published by Zmerli et al., where the higher stiffness of larger PDNPs compared to smaller ones was demonstrated, and the work of Ju et al., where the impact of the difference between large and small nanoparticles in the

Table 1. Summary of the Main Features of Differently-Sized PDNPs

ammonia/dopamine molar ratio	nanoparticle diameter [nm]	D_h [nm]	PDI	ζ-pot [mV]	absorbance at 808 nm [au]
23.20	145 ± 13	191.2 ± 1.6	0.02 ± 0.02	−39.8 ± 0.9	0.29 ± 0.03
17.40	186 ± 15	237.4 ± 4.5	0.04 ± 0.01	−46.1 ± 0.5	0.41 ± 0.02
14.50	204 ± 18	263.5 ± 6.8	0.05 ± 0.03	−46.7 ± 1.1	0.42 ± 0.04
11.60	299 ± 31	377.0 ± 1.8	0.11 ± 0.10	−43.1 ± 0.7	0.44 ± 0.05
8.70	426 ± 45	547.1 ± 24.6	0.02 ± 0.09	−42.8 ± 0.1	1.06 ± 0.05
5.80	522 ± 70	613.5 ± 46.1	0.24 ± 0.15	−44.4 ± 0.3	1.06 ± 0.04
4.35	710 ± 57	911.0 ± 72.5	0.17 ± 0.15	−47.6 ± 1.0	1.21 ± 0.07
2.90	957 ± 48	1095.0 ± 51.0	0.19 ± 0.07	−42.8 ± 0.4	1.46 ± 0.04

https://doi.org/10.1021/acsanm.1c04536
ACS Appl. Nano Mater. 2022, 5, 1702−1713

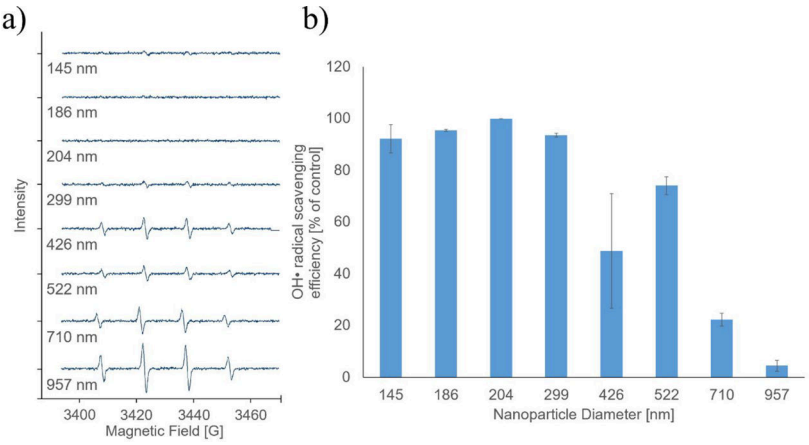

Figure 3. Analysis of PDNP antioxidant properties. (a) Representative EPR spectra of 500 μg/mL of PDNPs at various sizes. Typical four peaks corresponding to the spin adduct DMPO−OH resulting from reaction of the hydroxyl radicals with the spin trap DMPO are evident in the samples with weaker antioxidant properties. (b) $OH^{\bullet}$ radical scavenging efficiency of PDNPs at various sizes as a percentage of the number of radicals in the absence of nanoparticles (n = 3; for statistical analysis, please refer to Table S2).

hierarchical arrangement of protomolecules was revealed.[25,32] All of this evidence represents fundamental aspects to be taken into consideration in the case of prolonged in vivo treatments.[33−36]

3.3. Antioxidant properties. To evaluate the antioxidant properties, hydroxyl radicals were generated in situ exploiting the Fenton reaction ($Fe^{2+} + H_2O_2 \rightarrow Fe^{3+} + OH^{\bullet} + HO^{-}$). This reaction was chosen for its high $OH^{\bullet}$ radical generation reproducibility and efficiency.[37] The very short half-life of hydroxyl radicals requires the coupling of the spin-trap technique with EPR spectroscopy. For each of the differently sized classes of PDNPs, the EPR spectrum (Figure 3a) was obtained after 5 min from the start of the Fenton reaction. Quantitative results (Figure 3b) showed an $OH^{\bullet}$ radical scavenging efficiency of 92.22% for the smallest nanoparticles. As the diameter increases, the scavenging efficiency progressively decreases, up to the largest nanoparticles that show an $OH^{\bullet}$ radical scavenging efficiency of 4.52%. Nanoparticles with a diameter smaller than 300 nm showed a statistically significant increment in antioxidant capacity with respect to the largest nanoparticles ($p < 0.001$). Despite nanoparticles with a 426 nm diameter showing an antioxidant capacity with larger standard deviation, their antioxidant capacity was significantly lower than the four samples with smaller diameters (i.e., PDNPs at 145, 186, 204, and 299 nm; $p < 0.01$, Table S2). Furthermore, the antioxidant capacity of the 426 nm PDNPs is significantly higher ($p < 0.05$) than the nanoparticle with the largest diameter. The absence of a statistically significant difference in antioxidant capacity between the sample of 426 nm and the sample of 522 nm can be attributed to the small difference between the nanoparticle size and the relatively high standard deviation that the two diameter values show (i.e., 426.4 ± 45.2 and 522.1 ± 70.0 nm). Numerically speaking, by comparing the smallest to the largest nanoparticles, there is a decrement in the antioxidant capacity of 95.1%. Obtained results, in line with the work of Oh et al. on Prussian blue nanoparticles,[38] demonstrate that a higher surface/volume ratio, hence smaller nanoparticles, leads to stronger antioxidant properties, mostly because of a higher amount of functional groups exposed on the surface (i.e., catechol, amine, and imine in the case of PDA[14]).

3.4. NIR Photothermal Conversion. The heat generated by irradiation with a NIR laser source was measured using a thermal camera. For tests on both aqueous dispersions of PDNPs and brain tissue slices injected with nanoparticles, the procedure was carried out with the layout schematically shown in Figure 4a. As highlighted from thermal images acquired at different time points during NIR irradiation (representative images shown in Figure 4b and 4c), the average temperature increment observed in the entire examined domains, in the absence of PDNPs, was 0.4°C for the aqueous dispersion case and 0.6°C for the ex vivo experiments. Conversely, in the presence of nanoparticles, a consistent increment in temperature during irradiation was observed: in particular, as the PDNP diameter increases, the temperature increment within the entire experimental domain qualitatively increases.

Obtained quantitative data confirmed that an increment of size affects the photothermal conversion properties by enhancing the capability of the irradiated nanoparticles to heat the surrounding environment both in aqueous suspension (Figure 5a) and in brain tissue (Figure 5b). The trend of the tested concentrations and of the different laser powers is reported in Figure S6. Regarding irradiation of the aqueous dispersion, after 120 s at the highest concentration tested, the largest nanoparticles showed an average temperature increment that was about 40% higher with respect to that shown by the smaller nanoparticles. In the case of the irradiated cow brain tissue, after 120 s at the highest laser power tested, again by comparing the largest nanoparticles with the smallest ones, the observed difference in the average temperature increment was about 51%.

The enhancement in photothermal conversion ability along with the increment of the size is in line with the increment in absorbance values at 808 nm (Figure S3), and it is the opposite behavior with respect to the trend occurring during irradiation of nanoparticles that exploit the surface plasmon resonance, such as gold nanostructures.[39−41] Furthermore, other studies exploiting PDNPs for photothermal therapy have highlighted different results:[4,13] for example, in the works of Liu et al. and Zhuang et al., NIR irradiation of an aqueous dispersion of nanoparticles (100 μg/mL) resulted into a 2-fold maximum temperature increment with respect to our results;[40,42] in both cases, however, the laser power chosen was about 4 times higher, 2 W cm^{-1} instead of 0.541 W cm^{-1}.

https://doi.org/10.1021/acsanm.1c04536
ACS Appl. Nano Mater. 2022, 5, 1702−1713

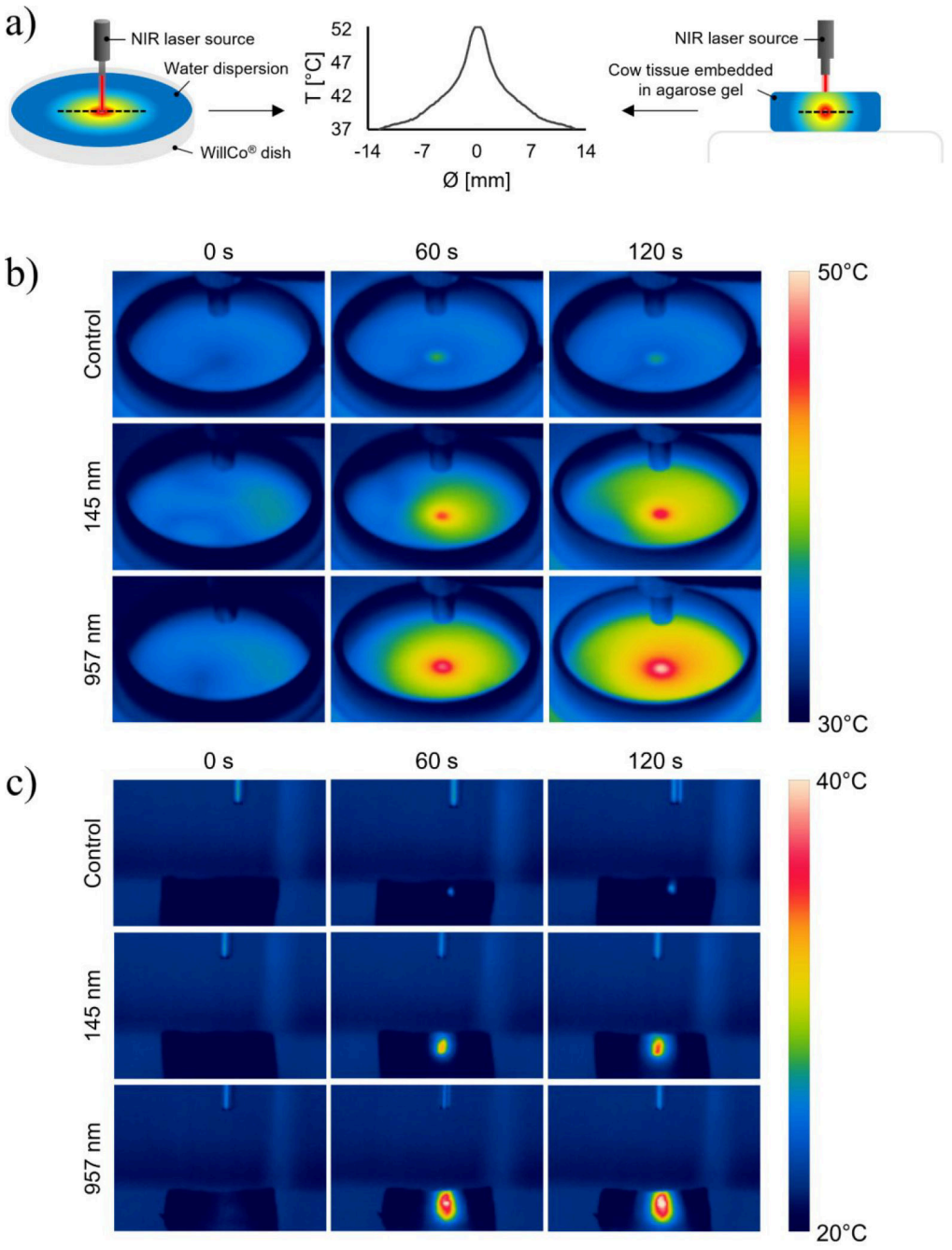

Figure 4. Photothermal conversion ability analysis. (a) Diagram of the settings used for thermal data acquisition. (Left) Three-dimensional representation of the NIR laser source irradiating a WillCo dish containing the PDNP aqueous dispersions; (right) two-dimensional front-view representation of the NIR laser source irradiating a slice of cow brain tissue embedded in agarose gel and containing the injected PDNPs; (center) representative plot of the data obtained from the segments (dashed lines) depicted in the just-mentioned schemes. (b) Representative thermal images acquired at different time points of NIR irradiation of aqueous dispersions of PDNPs. (c) Representative thermal images acquired at different time points of NIR irradiation of PDNPs injected in cow brain tissues.

We introduced a computational model to derive quantitative insights from the aforementioned experiments with aqueous dispersions of nanoparticles. A model schematic is shown in Figure 6a (cross-sectional cut view, owing to axisymmetry). A few key dimensions are explicitly added for the WillCo dish domain containing PDNPs and for the NIR spot for ease of presentation. Boundary conditions are represented by corresponding symbols: input power W_{NIR} points to the NIR spot, the fixed-temperature lower boundary is linked to T_{plate}, and thermal exchange between the remaining boundaries and the external environment is given by T_{room}. Moreover, for the sake of illustration, a temperature field resulting from NIR irradiation (contour plot, 3D-cut view) is shown in the top-left inset, and a complementary time evolution of temperature on the upper surface of the WillCo dish liquid domain (contour plot, top view) is shown in Video S1. Finally, Figure 6b shows model results (solid curves) versus corresponding experimental data sets (points ± bars, for mean ± standard deviation).

The heat transfer coefficient resulting from calibration was $h \approx 1.29 \times 10^2$ W m^{-2} K^{-1}, while the following values were

https://doi.org/10.1021/acsanm.1c04536
ACS Appl. Nano Mater. 2022, 5, 1702−1713

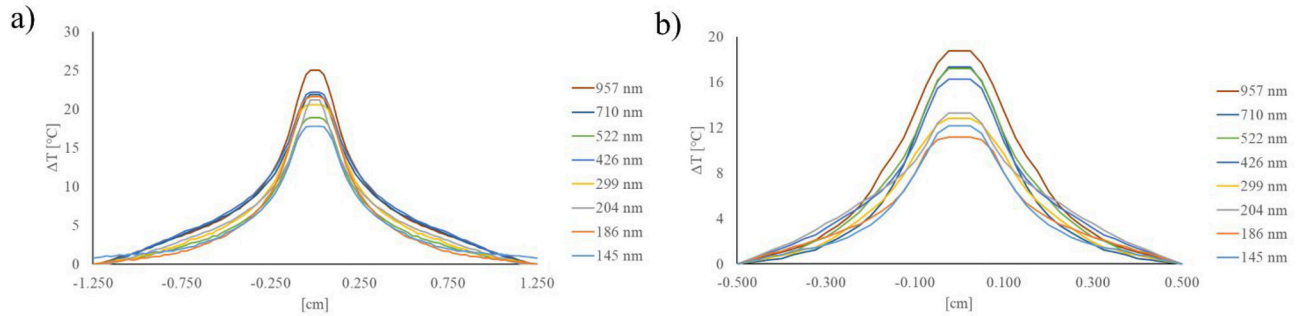

Figure 5. Photothermal conversion analysis. (a) Temperature increment profiles (along the domain highlighted in Figure 4a) of aqueous dispersions of differently sized PDNPs at 1 mg/mL after 120 s of irradiation with NIR laser. (b) Temperature increment profile (along the domain highlighted in Figure 4a) after 120 s of irradiation with NIR laser of 25 μg of differently sized PDNPs injected in cow brain tissue.

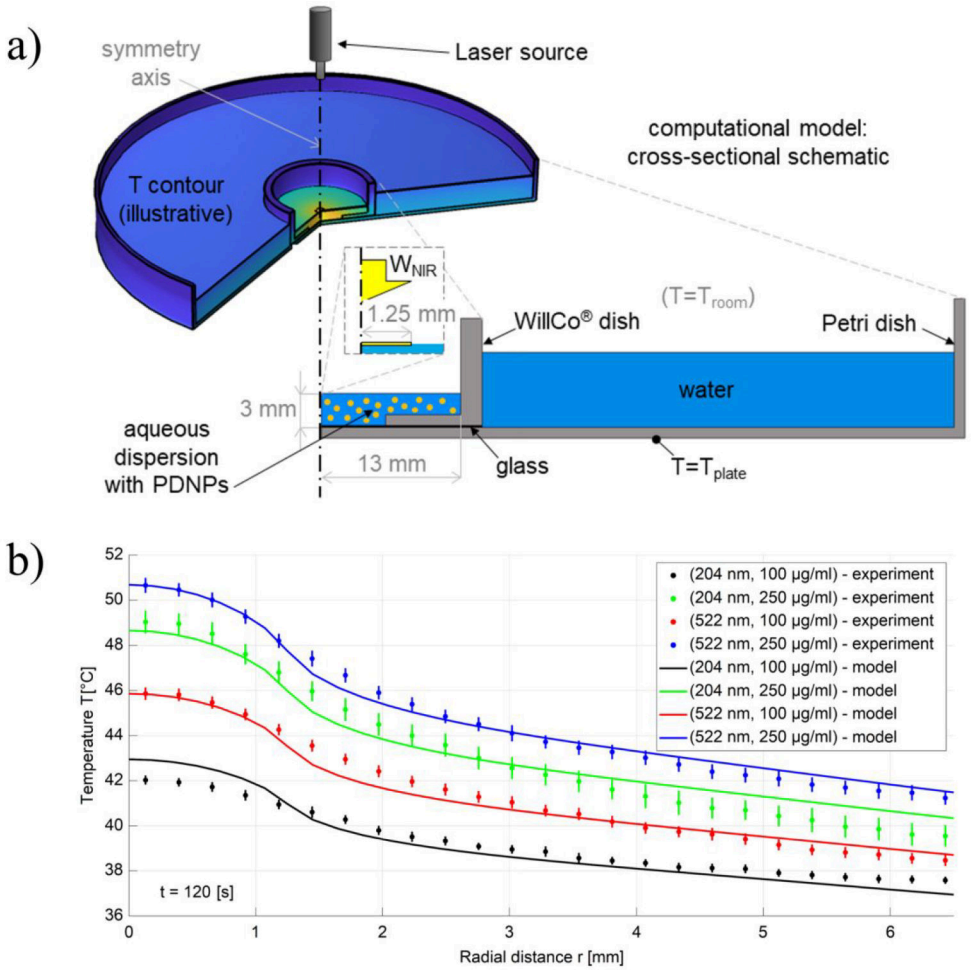

Figure 6. Computational model: (a) Schematic and (b) numerical model results (solid curves) versus corresponding experimental data sets (n = 3).

obtained for the (normalized) absorption coefficient: $\alpha = 1$ (by definition) for the 204 nm/100 μg/mL pair, $\alpha \approx 1.25$ for 522 nm/100 μg/mL, $\alpha \approx 1.50$ for 204 nm/250 μg/mL, and $\alpha \approx 1.69$ for 522 nm/250 μg/mL. Taking the 204 nm/100 μg/mL dispersion as a reference sample, the above quantification suggests that the photothermal conversion capability could be enhanced more significantly by an increase in concentration rather than in size (1.50- vs 1.25-fold increase, respectively). However, the enhancement factors seem to depend on the reference sample (indeed, for the considered increase in concentration, the enhancement factors were 1.50 and 1.69/1.25 $\approx$ 1.35 for the 204 and 522 nm diameter PDNPs, respectively). Stronger claims, however, should be based on more exhaustive investigations since more accurate results could be obtained by enriching experimental methods and physical submodeling (e.g., by also considering reflection and back-scattering effects based on the effective availability of experimental values for the corresponding calibration not to augment uncertainty).

In particular, more refined experiments in a thermally controlled environment and the obtainment of nondimensional absorbance values (consistent with absorbance definition, as the

https://doi.org/10.1021/acsanm.1c04536
ACS Appl. Nano Mater. 2022, 5, 1702−1713

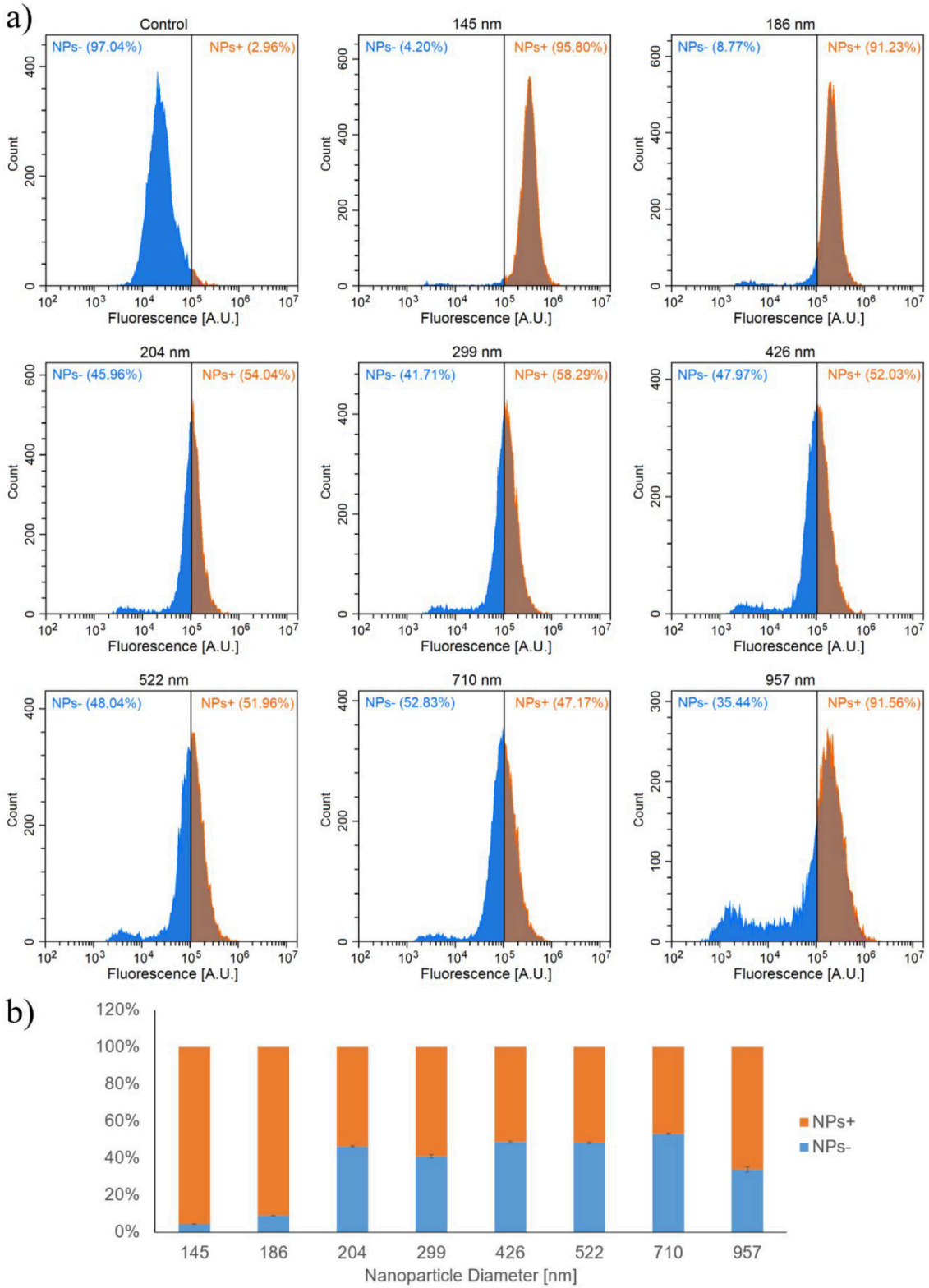

Figure 7. Flow cytometry analysis of U-87 MG cells incubated with 100 μg/mL of differently sized DiO-stained PDNPs for 72 h: orange, nanoparticles-positive cells (NPs+); blue, nanoparticles-negative cells (NPs−). (a) Representative flow cytometry plots showing fluorescence levels of cells in different experimental conditions; (b) percentages of NPs+ and NPs− cells for each experimental condition (n = 3; for statistical analysis, please refer to Table S3).

ratio between incident and transmitted power, up to using the log 10 scale[44]) would permit one to also estimate the photothermal conversion efficiency (by using methods similar to those in refs 43 and 44). Nonetheless, the developed model positively complemented the related experiments, and further developments could support more refined experimental investigations, in terms of both study design and result

https://doi.org/10.1021/acsanm.1c04536
ACS Appl. Nano Mater. 2022, 5, 1702−1713

interpretation, toward protocols and therapy control for prospective clinical applications.

3.5. PDNP Interactions with U-87 MG Cells. Regarding interactions with cells, the effect on cellular proliferation and viability was first assessed. For each differently sized PDNP, U-87 MG cells were treated with increasing concentrations of nanoparticles (0, 100, 250, and 500 μg/mL) and analyzed after 72 h through the PicoGreen assay (Figure S7). Fluorescence levels, indicative of cell number, did not show any statistically significant differences ($p > 0.05$) with respect to the corresponding control, except for the largest nanoparticles at the highest concentration tested (957 nm particles, 500 μg/mL). In this case, a statistically significant decrease in viability was observed (about 50%, $p < 0.001$).

PDNP biocompatibility has been already widely demonstrated in the literature, on both in vitro and in vivo models;[2−4] however, some works pointed out the toxic effects of PDNPs: for example, Sun et al. showed a neurotoxic effect on zebrafish at concentrations higher than 500 μg/mL, while Nieto et al. highlighted an increment in cytotoxic effect along with a decrement in diameter.[45−47] This discrepancies can be attributed, besides to the relatively high concentrations used, to the difference in the adopted protocol for evaluation of the cytotoxic effects, and to the specific sensitivity of different cell types to nanomaterials.[48]

Cellular uptake was assessed through flow cytometry (Figure 7) and confocal microscopy (Figures 8 and S8): both techniques confirmed the trend of a decrement of the cellular uptake along with the increment of the average diameter.[49,50] A progressive increment of nanoparticle internalization, from 47.2% nanoparticles-associated cells to 64.6% nanoparticles-associated cells, was found for nanoparticles with decreasing diameters, from 957 to 204 nm. Below 200 nm in diameter, the internalization remarkably increases, reaching a value of 95.8% nanoparticles-associated cells for the smallest PDNPs. Only the largest nanoparticles showed an inversion of this trend: this behavior is probably due to the lower stability in cell culture medium with respect to nanoparticle characterized by smaller sizes.[51,52] Complete analysis of the differences in terms of cell uptake according to different PDNP diameter sizes is provided in Table S3.

Confocal microscopy imaging, with the exploitation of the DiI temperature-sensitive dye, allowed analysis of the intracellular temperature increment upon PDNP incubation and NIR treatment. The smallest nanoparticles (145 nm PDNPs) produced an increase in temperature of 2.8 ± 0.8 °C, while the largest nanoparticles (957 nm PDNPs) produced an increase in temperature of 5.2 ± 1.3 °C (Figure 9); these data, in agreement with all previously described results, confirm the enhancement of the photothermal conversion ability along the increment in diameter size.

CONCLUSIONS

The results of this work demonstrate how the size impacts biocompatibility, cell uptake, NIR absorbance, degradation behavior, antioxidant properties, and photothermal conversion ability of PDNPs. We provided useful information to finely tune the PDNP features for the intended application: small nanoparticles, with a diameter of less than 200 nm, appear to be the best choice for drug delivery applications thanks to their higher internalization extent. Furthermore, these nanoparticles, having a higher antioxidant capacity, are preferable as agents for treating cells characterized by strong oxidative stress, as in the case of neurodegenerative pathologies.[19] Larger nanoparticles are instead preferable for photothermal therapy treatments: indeed, as evidenced by our tests on U-87 cells, PDNPs of 957

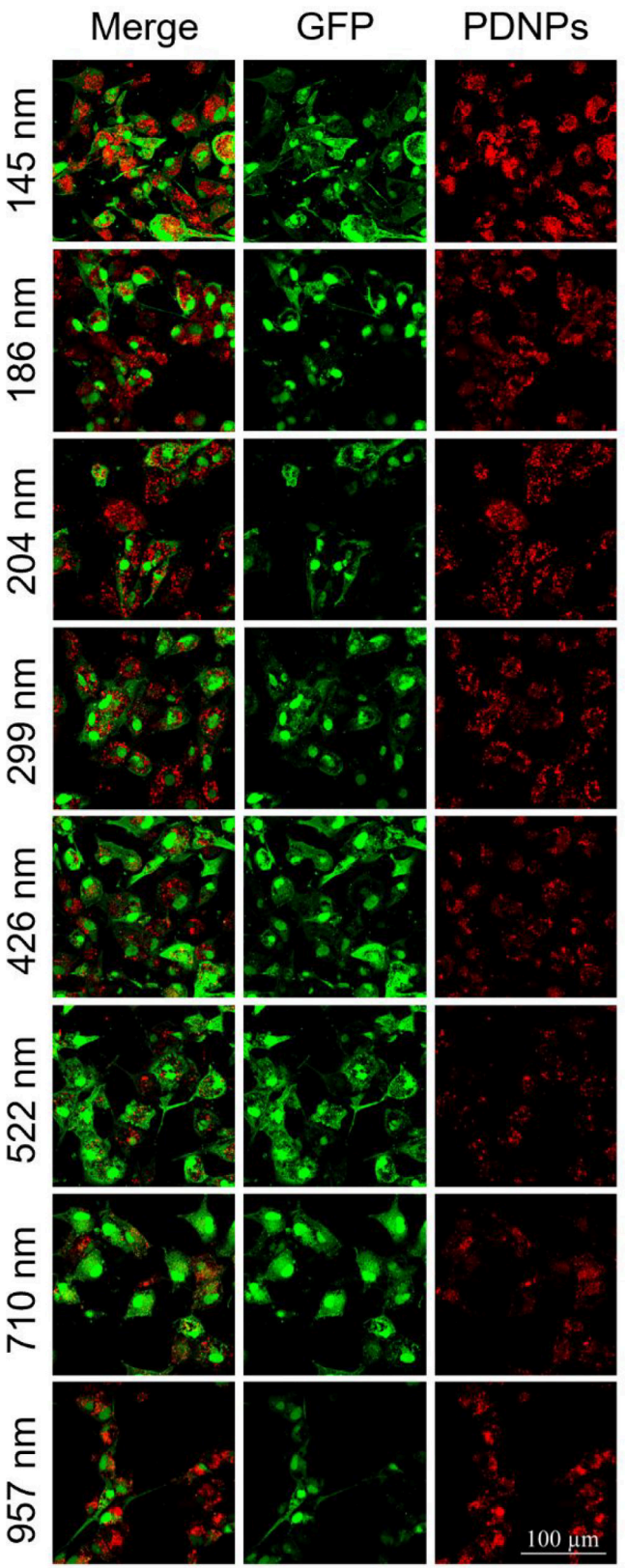

Figure 8. Representative confocal images of U-87 MG/GFP cells incubated with 100 μg/mL of differently sized DiI-stained PDNPs for 72 h.

https://doi.org/10.1021/acsanm.1c04536
ACS Appl. Nano Mater. 2022, 5, 1702−1713

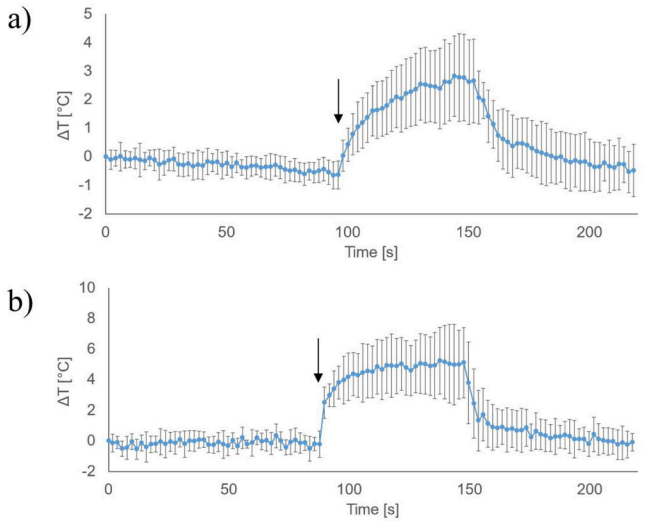

Figure 9. Analysis of the intracellular temperature variation (ΔT) in U-87 MG cells treated with 100 μg/mL PDNPs during NIR stimulation. (a and b) Results for PDNPs of 145 and 957 nm nominal diameter, respectively (black arrow indicates the start of NIR irradiation; $n = 3$).

nm in diameter can raise the intracellular temperature over 42°C, suitable for hyperthermia.[53] Owing to the improved photothermal transduction efficiency, PDNPs with diameter > 900 nm can be also considered for controlled drug release applications;[54] however, the relatively big size of these particles may limit their exploitation for brain delivery applications due to the expected low blood−brain barrier (BBB) crossing efficiency. In conclusion, all of the collected data provide useful knowledge to tailor the most appropriate PDNP size according to the intended biomedical application.

■ ASSOCIATED CONTENT

Supporting Information

The Supporting Information is available free of charge at https://pubs.acs.org/doi/10.1021/acsanm.1c04536.

Figures showing the hydrodynamic diameter distributions, zeta potential distributions, UV−vis absorbance values at 808 nm, short-term stability analysis, nanoparticle degradation analysis, photothermal conversion analysis, viability assay, and 3D confocal imaging; tables with detailed statistical analyses (PDF)

A video showing representative temperature variation upon NIR+PNDPs stimulation (MP4)

■ AUTHOR INFORMATION

Corresponding Authors

Alessio Carmignani − *Istituto Italiano di Tecnologia, 56025 Pontedera, Italy; Sant'Anna School of Advanced Studies, The Biorobotics Institute, 56025 Pontedera, Italy;* orcid.org/0000-0002-6316-3478; Email: alessio.carmignani@iit.it

Gianni Ciofani − *Istituto Italiano di Tecnologia, 56025 Pontedera, Italy;* orcid.org/0000-0003-1192-3647; Email: gianni.ciofani@iit.it

Authors

Matteo Battaglini − *Istituto Italiano di Tecnologia, 56025 Pontedera, Italy*

Edoardo Sinibaldi − *Bioinspired Soft Robotics, Istituto Italiano di Tecnologia, 16163 Genova, Italy;* orcid.org/0000-0002-9755-3431

Attilio Marino − *Istituto Italiano di Tecnologia, 56025 Pontedera, Italy;* orcid.org/0000-0002-3290-494X

Veronica Vighetto − *Department of Applied Science and Technology, Politecnico di Torino, 10129 Torino, Italy*

Valentina Cauda − *Department of Applied Science and Technology, Politecnico di Torino, 10129 Torino, Italy;* orcid.org/0000-0003-2382-1533

Complete contact information is available at: https://pubs.acs.org/10.1021/acsanm.1c04536

Author Contributions

The manuscript was written through the contributions of all authors. All authors have given approval to the final version of the manuscript.

Notes

The authors declare no competing financial interest.

■ ACKNOWLEDGMENTS

The authors kindly thank Francesco Martini (Abinsula, Italy) for assistance in extracting and processing the thermal imaging data.

■ REFERENCES

(1) Chakravarthy, S.; Balasubramani, P. P.; Mandali, A.; Jahanshahi, M.; Moustafa, A. A. The many facets of dopamine: Toward an integrative theory of the role of dopamine in managing the body's energy resources. *Physiol. Behav.* **2018**, *195*, 128−141.

(2) Ju, K. Y.; Lee, Y.; Lee, S.; Park, S. B.; Lee, J. K. Bioinspired polymerization of dopamine to generate melanin-like nanoparticles having an excellent free-radical-scavenging property. *Biomacromolecules* **2011**, *12* (3), 625−632.

(3) Ku, S. H.; Ryu, J.; Hong, S. K.; Lee, H.; Park, C. B. General functionalization route for cell adhesion on non-wetting surfaces. *Biomaterials* **2010**, *31* (9), 2535−2541.

(4) Liu, Y.; Ai, K.; Liu, J.; Deng, M.; He, Y.; Lu, L. Dopamine-melanin colloidal nanospheres: An efficient near-infrared photothermal therapeutic agent for in vivo cancer therapy. *Adv. Mater.* **2013**, *25* (9), 1353−1359.

(5) Yokel, R. A.; Au, T. C.; MacPhail, R.; Hardas, S. S.; Butterfield, D. A.; Sultana, R.; Goodman, M.; Tseng, M. T.; Dan, M.; Haghnazar, H.; Unrine, J. M.; Graham, U. M.; Wu, P.; Grulke, E. A. Distribution, elimination, and biopersistence to 90 days of a systemically introduced 30 nm ceria-engineered nanomaterial in rats. *Toxicol. Sci.* **2012**, *127* (1), 256−268.

(6) Bettinger, C. J.; Bruggeman, J. P.; Misra, A.; Borenstein, J. T.; Langer, R. Biocompatibility of biodegradable semiconducting melanin films for nerve tissue engineering. *Biomaterials* **2009**, *30* (17), 3050−3057.

(7) Napolitano, A.; Pezzella, A.; Vincensi, M. R.; Prota, G. Oxidative degradation of melanins to pyrrole acids: A model study. *Tetrahedron* **1995**, *51* (20), 5913−5920.

(8) Bao, X.; Zhao, J.; Sun, J.; Hu, M.; Yang, X. Polydopamine Nanoparticles as Efficient Scavengers for Reactive Oxygen Species in Periodontal Disease. *ACS Nano* **2018**, *12* (9), 8882−8892.

(9) Jiang, X.; Wang, Y.; Li, M. Selecting water-alcohol mixed solvent for synthesis of polydopamine nano-spheres using solubility parameter. *Sci. Rep.* **2014**, *4*, 6070.

(10) Djermane, R.; Nieto, C.; Vargas, J. C.; Vega, M. A.; Martin del Valle, E. Insight into the influence of the polymerization time of polydopamine nanoparticles on their size, surface properties and nanomedical applications. *Polym. Chem.* **2022**, *13*, 235.

(11) Liu, Y.; Ai, K.; Lu, L. Polydopamine and its derivative materials: Synthesis and promising applications in energy, environmental, and biomedical fields. *Chem. Rev.* **2014**, *114*, 5057.

(12) Cheng, W.; Zeng, X.; Chen, H.; Li, Z.; Zeng, W.; Mei, L.; Zhao, Y. Versatile Polydopamine Platforms: Synthesis and Promising Applications for Surface Modification and Advanced Nanomedicine. *ACS Nano* **2019**, *13*, 8537.
(13) Zeng, X.; Luo, M.; Liu, G.; Wang, X.; Tao, W.; Lin, Y.; Ji, X.; Nie, L.; Mei, L. Polydopamine-Modified Black Phosphorous Nanocapsule with Enhanced Stability and Photothermal Performance for Tumor Multimodal Treatments. *Adv. Sci.* **2018**, *5*, 1800510.
(14) Zhao, H.; Zeng, Z.; Liu, L.; Chen, J.; Zhou, H.; Huang, L.; Huang, J.; Xu, H.; Xu, Y.; Chen, Z.; Wu, Y.; Guo, W.; Wang, J. H.; Wang, J.; Liu, Z. Polydopamine nanoparticles for the treatment of acute inflammation-induced injury. *Nanoscale* **2018**, *10* (15), 6981−6991.
(15) Srivastava, A. K.; Roy Choudhury, S.; Karmakar, S. Melatonin/polydopamine nanostructures for collective neuroprotection-based Parkinson's disease therapy. *Biomater. Sci.* **2020**, *8*, 1345.
(16) Maziukiewicz, D.; Grześkowiak, B. F.; Coy, E.; Jurga, S.; Mrówczýnski, R. NDs@PDA@ICG conjugates for photothermal therapy of glioblastoma multiforme. *Biomimetics* **2019**, *4*, 3.
(17) Cheng, Y.; Zhang, S.; Kang, N.; Huang, J.; Lv, X.; Wen, K.; Ye, S.; Chen, Z.; Zhou, X.; Ren, L. Polydopamine-Coated Manganese Carbonate Nanoparticles for Amplified Magnetic Resonance Imaging-Guided Photothermal Therapy. *ACS Appl. Mater. Interfaces* **2017**, *9*, 19296.
(18) Ding, F.; Gao, X.; Huang, X.; Ge, H.; Xie, M.; Qian, J.; Song, J.; Li, Y.; Zhu, X.; Zhang, C. Polydopamine-coated nucleic acid nanogel for siRNA-mediated low-temperature photothermal therapy. *Biomaterials* **2020**, *245*, 119976.
(19) Battaglini, M.; Marino, A.; Carmignani, A.; Tapeinos, C.; Cauda, V.; Ancona, A.; Garino, N.; Vighetto, V.; La Rosa, G.; Sinibaldi, E.; Ciofani, G. Polydopamine Nanoparticles as an Organic and Biodegradable Multitasking Tool for Neuroprotection and Remote Neuronal Stimulation. *ACS Appl. Mater. Interfaces* **2020**, *12*, 35782.
(20) Ambekar, R. S.; Kandasubramanian, B. A polydopamine-based platform for anti-cancer drug delivery. *Biomaterials Science.* **2019**, *7*, 1776.
(21) Mayerhöfer, T. G.; Pahlow, S.; Popp, J. The Bouguer-Beer-Lambert Law: Shining Light on the Obscure. *ChemPhysChem.* **2020**, *21*, 2029.
(22) Wunderlich, B. Quantitative thermal analysis of macromolecular glasses and crystals. *Thermochim. Acta* **1985**, *92*, 15.
(23) Marino, A.; Camponovo, A.; Degl'Innocenti, A.; Bartolucci, M.; Tapeinos, C.; Martinelli, C.; De Pasquale, D.; Santoro, F.; Mollo, V.; Arai, S.; Suzuki, M.; Harada, Y.; Petretto, A.; Ciofani, G. Multifunctional Temozolomide-loaded lipid superparamagnetic nanovectors: Dual targeting and disintegration of glioblastoma spheroids by synergic chemotherapy and hyperthermia treatment. *Nanoscale* **2019**, *11*, 21227.
(24) Ai, K.; Liu, Y.; Ruan, C.; Lu, L.; Lu, G. Sp2 C-dominant N-doped carbon sub-micrometer spheres with a tunable size: A versatile platform for highly efficient oxygen-reduction catalysts. *Adv. Mater.* **2013**, *25*, 998.
(25) Ju, K. Y.; Fischer, M. C.; Warren, W. S. Understanding the Role of Aggregation in the Broad Absorption Bands of Eumelanin. *ACS Nano* **2018**, *12*, 12050.
(26) Nohl, H.; Gille, L. Lysosomal ROS formation. *Redox Report.* **2005**, *10*, 199.
(27) Lin, M. T.; Beal, M. F. Mitochondrial dysfunction and oxidative stress in neurodegenerative diseases. *Nature.* **2006**, *443*, 787.
(28) Islam, M. T. Oxidative stress and mitochondrial dysfunction-linked neurodegenerative disorders. *Neurological Research.* **2017**, *39*, 73.
(29) Li, X.; Lin, H.; Zhang, X.; Jaspers, R. T.; Yu, Q.; Ji, Y.; Forouzanfar, T.; Wang, D.; Huang, S.; Wu, G. Notoginsenoside R1 attenuates oxidative stress-induced osteoblast dysfunction through JNK signalling pathway. *J. Cell. Mol. Med.* **2021**, *25*, 11278.
(30) Hadipour Moghaddam, S. P.; Mohammadpour, R.; Ghandehari, H. In vitro and in vivo evaluation of degradation, toxicity, biodistribution, and clearance of silica nanoparticles as a function of size, porosity, density, and composition. *J. Controlled Release* **2019**, *311-312*, 1−15.
(31) Yamada, H.; Urata, C.; Aoyama, Y.; Osada, S.; Yamauchi, Y.; Kuroda, K. Preparation of colloidal mesoporous silica nanoparticles with different diameters and their unique degradation behavior in static aqueous systems. *Chem. Mater.* **2012**, *24* (8), 1462.
(32) Zmerli, I.; Michel, J. P.; Makky, A. Bioinspired polydopamine nanoparticles: Synthesis, nanomechanical properties, and efficient PEGylation strategy. *J. Mater. Chem. B* **2020**, *8*, 4489.
(33) Cho, M.; Cho, W. S.; Choi, M.; Kim, S. J.; Han, B. S.; Kim, S. H.; Kim, H. O.; Sheen, Y. Y.; Jeong, J. The impact of size on tissue distribution and elimination by single intravenous injection of silica nanoparticles. *Toxicol. Lett.* **2009**, *189* (3), 177.
(34) Xie, G.; Sun, J.; ZhonG, G.; Shi, L.; ZhanG, D. Biodistribution and toxicity of intravenously administered silica nanoparticles in mice. *Arch. Toxicol.* **2010**, *84* (3), 183.
(35) Lee, J. A.; Kim, M. K.; Paek, H. J.; Kim, Y. R.; Kim, M. K.; Lee, J. K.; Jeong, J.; Choi, S. J. Tissue distribution and excretion kinetics of orally administered silica nanoparticles in rats. *Int. J. Nanomed.* **2014**, *9*, 251−260.
(36) Hoshyar, N.; Gray, S.; Han, H.; Bao, G. The effect of nanoparticle size on in vivo pharmacokinetics and cellular interaction. *Nanomedicine.* **2016**, *11*, 673.
(37) Trouillas, P.; Calliste, C. A.; Allais, D. P.; Simon, A.; Marfak, A.; Delage, C.; Duroux, J. L. Antioxidant, anti-inflammatory and antiproliferative properties of sixteen water plant extracts used in the Limousin countryside as herbal teas. *Food Chem.* **2003**, *80* (3), 399−407.
(38) Oh, H.; Lee, J. S.; Sung, D.; Lee, J. H.; Moh, S. H.; Lim, J. M.; Choi, W. Il. Synergistic antioxidant activity of size controllable chitosan-templated Prussian blue nanoparticle. *Nanomedicine* **2019**, *14* (19), 2567.
(39) Du, B.; Ma, C.; Ding, G.; Han, X.; Li, D.; Wang, E.; Wang, J. Cooperative Strategies for Enhancing Performance of Photothermal Therapy (PTT) Agent: Optimizing Its Photothermal Conversion and Cell Internalization Ability. *Small* **2017**, *13* (13), 1603275.
(40) Liu, H.; Liu, T.; Li, L.; Hao, N.; Tan, L.; Meng, X.; Ren, J.; Chen, D.; Tang, F. Size dependent cellular uptake, in vivo fate and light-heat conversion efficiency of gold nanoshells on silica nanorattles. *Nanoscale* **2012**, *4* (11), 3523.
(41) Norouzi, H.; Khoshgard, K.; Akbarzadeh, F. In vitro outlook of gold nanoparticles in photo-thermal therapy: a literature review. *Lasers in Medical Science.* **2018**, *33*, 917.
(42) Zhuang, H.; Su, H.; Bi, X.; Bai, Y.; Chen, L.; Ge, D.; Shi, W.; Sun, Y. Polydopamine Nanocapsule: A Theranostic Agent for Photoacoustic Imaging and Chemo-Photothermal Synergistic Therapy. *ACS Biomater. Sci. Eng.* **2017**, *3*, 1799.
(43) Ge, R.; Lin, M.; Li, X.; Liu, S.; Wang, W.; Li, S.; Zhang, X.; Liu, Y.; Liu, L.; Shi, F.; Sun, H.; Zhang, H.; Yang, B. Cu^{2+}-loaded polydopamine nanoparticles for magnetic resonance imaging-guided pH- and near-infrared-light-stimulated thermochemotherapy. *ACS Appl. Mater. Interfaces* **2017**, *9* (23), 19706−19716.
(44) Zmerli, I.; Ibrahim, N.; Cressey, P.; Denis, S.; Makky, A. Design and Synthesis of New PEGylated Polydopamine-Based Nanoconstructs Bearing ROS-Responsive Linkers and a Photosensitizer for Bimodal Photothermal and Photodynamic Therapies against Cancer. *Mol. Pharm.* **2021**, *18*, 3623.
(45) Nieto, C.; Vega, M. A.; Marcelo, G.; Martín Del Valle, E. M. Polydopamine nanoparticles kill cancer cells. *RSC Adv.* **2018**, *8*, 36201.
(46) Nieto, C.; Vega, M. A.; Enrique, J.; Marcelo, G.; Del Valle, E. M. M. Size matters in the cytotoxicity of polydopamine nanoparticles in different types of tumors. *Cancers (Basel)* **2019**, *11*, 1679.
(47) Sun, M.; Cao, Y.; Sun, Q.; Ren, X.; Hu, J.; Sun, Z.; Duan, J. Exposure to polydopamine nanoparticles induces neurotoxicity in the developing zebrafish. *NanoImpact* **2021**, *24*, 100353.
(48) Kroll, A.; Dierker, C.; Rommel, C.; Hahn, D.; Wohlleben, W.; Schulze-Isfort, C.; Göbbert, C.; Voetz, M.; Hardinghaus, F.; Schnekenburger, J. Cytotoxicity screening of 23 engineered nanomaterials using a test matrix of ten cell lines and three different assays. *Part. Fibre Toxicol.* **2011**, *8*, 9.

https://doi.org/10.1021/acsanm.1c04536
ACS Appl. Nano Mater. 2022, 5, 1702−1713

(49) Kulkarni, S. A.; Feng, S. S. Effects of particle size and surface modification on cellular uptake and biodistribution of polymeric nanoparticles for drug delivery. *Pharm. Res.* **2013**, *30* (10), 2512.
(50) Lu, F.; Wu, S. H.; Hung, Y.; Mou, C. Y. Size effect on cell uptake in well-suspended, uniform mesoporous silica nanoparticles. *Small* **2009**, *5* (12), 1408.
(51) Shin, H. R.; Kwak, M.; Lee, T. G.; Lee, J. Y. Quantifying the level of nanoparticle uptake in mammalian cells using flow cytometry. *Nanoscale* **2020**, *12* (29), 15743.
(52) Givan, A. L. Flow cytometry: an introduction. *Methods in molecular biology (Clifton, N.J.)*. **2011**, *699*, 1.
(53) Tapeinos, C.; Marino, A.; Battaglini, M.; Migliorin, S.; Brescia, R.; Scarpellini, A.; De Julián Fernández, C.; Prato, M.; Drago, F.; Ciofani, G. Stimuli-responsive lipid-based magnetic nanovectors increase apoptosis in glioblastoma cells through synergic intracellular hyperthermia and chemotherapy. *Nanoscale* **2019**, *11*, 72.
(54) Nikjoo, D.; van der Zwaan, I.; Brülls, M.; Tehler, U.; Frenning, G. Hyaluronic acid hydrogels for controlled pulmonary drug delivery—a particle engineering approach. *Pharmaceutics* **2021**, *13*, 1878.

NOTE ADDED AFTER ASAP PUBLICATION

Due to a production error, this paper was published ASAP on January 14, 2022, with an error in the title. The corrected version was reposted on January 18, 2022.

https://doi.org/10.1021/acsanm.1c04536
ACS Appl. Nano Mater. 2022, 5, 1702−1713